Materials & Design 244 (2024) 113171

Contents lists available at ScienceDirect

Materials & Design

journal homepage: www.elsevier.com/locate/matdes

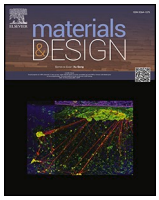

Impact of scan strategy on principal stresses in laser powder bed fusion

Jakob Schröder [a,*], Tobias Fritsch [a], Vladimir Luzin [b,c], Bruno Ferrari [a], Juan Simón-Muzás [a], Alexander Evans [a], Giovanni Bruno [a,d]

[a] Bundesanstalt für Materialforschung und -prüfung, Unter den Eichen 87, 12205 Berlin, Germany
[b] Australia Nuclear Science and Technology Organisation, New Illawara Rd, Lucas Heights, NSW 2234, Australia
[c] School of Engineering, The University of Newcastle, Callaghan, NSW 2234, Australia
[d] Universität Potsdam, Institut für Physik und Astronomie, Karl-Liebknecht-Str. 24-25, 14476 Potsdam, Germany

ARTICLE INFO

Keywords:
Additive Manufacturing
Laser Powder Bed Fusion
Electron Backscatter Diffraction
Neutron Diffraction
Residual Stress
Principal Stress

ABSTRACT

Additive manufacturing techniques, such as laser powder bed fusion (PBF-LB), are well known for their exceptional freedom in part design. However, these techniques are also characterized by the development of large thermal gradients during production and thus residual stress (RS) formation in produced parts. In this context, neutron diffraction enables the non-destructive characterization of the bulk RS distribution. By control of the thermal gradients in the powder-bed plane by scan strategy variation we study the impact of in-process scan strategy variations on the microstructure and the three-dimensional distribution of RS. Microstructural analysis by means of electron backscatter diffraction reveals sharp microstructure transitions at the interfaces ranging from 100-200 μm. The components of the RS tensor are determined by means of neutron diffraction and the principal stress directions and magnitudes are determined by eigenvalue decomposition. We find that the distribution of RS in the powder-bed plane corresponds to the underlying scan strategy. When the alternating scan vectors align with the x- and y sample coordinate axes, the principal stress directions co-align. In the present geometry, nearly transverse isotropic stress states develop when the scan vectors are either aligned 45° between x and y or continuously rotated by 67° between each layer.

1. Introduction

Additive manufacturing (AM) processes, such as laser powder bed fusion (PBF-LB), facilitate the production of complex-shaped parts [1]. This is enabled by the localized melting of feedstock powder and build-up of the part in a layer-by-layer fashion [1]. Due to this processing strategy, PBF-LB offers immense freedom in part design [1]. Therefore, industry sectors demanding complex geometries and/or weight reduction in high-temperature applications, such as the gas turbine and aerospace industry, show significant interest in the development of PBF-LB [2]. Due to its excellent weldability [3] coupled with the potential for high-temperature application up to 650 °C [4], the Ni-based precipitation-hardened alloy Inconel 718 (IN718) is an established candidate for PBF-LB processing [5]. In essence, this alloy has a face-centered cubic (fcc) matrix, strengthened by so-called γ'' (Ni_3Nb) and γ' (Ni_3(Al, Ti)) intermetallic precipitates to achieve excellent mechanical properties at high temperature [6]. However, some complications arise from the localized laser melting in the PBF-LB production of IN718. On the one hand, localized melting creates large thermal gradients during production [7,8]. In consequence, these thermal gradients lead to the build-up of thermal stress, which result in residual stress (RS) in the manufactured parts [7,8]. On the other hand, localized melting facilitates rapid solidification, characterized by competitive cell growth at the sub grain level [9]. This rapid cell-like solidification is accompanied by micro segregation and dislocation entanglement at cell walls [9]. At grain scale the large thermal gradients often favor the formation of large columnar grains with crystallographic texture [9,10].

The benefit of the localized processing is that the microstructure and the texture can be tailored. During solidification, the fcc crystals align with their ⟨100⟩ growth direction in the largest direction of heat flow [11]. In this context, the laser beam parameters have a direct influence on the melt pool shape and size, affecting the dominant direction of heat flow [10]. Therefore, characteristic microstructures ranging from lamellar, single-crystal-like to polycrystalline-like can be achieved by variation of the scanning velocity and the laser power [10]. In addition to the laser beam parameters, different scan strategies can be applied to

* Corresponding author.
E-mail address: Jakob.Schroeder@bam.de (J. Schröder).

https://doi.org/10.1016/j.matdes.2024.113171
Received 24 May 2024; Received in revised form 5 July 2024; Accepted 13 July 2024
Available online 24 July 2024

tailor the microstructure and the texture [9,12,13]. Like so, the orientation of the crystals perpendicular to the build direction can be controlled without changing the melt pool shape and size [13]. Besides controlling the microstructure and the texture, these factors also facilitate the design of functionally graded parts [14]. Through in-process variation of the laser power Popovich et al. [14] changed the microstructure and the texture along the build direction of parts. Hence, the resulting spatial distribution of the material properties can be tailored, offering unique capabilities for the design of structural components.

Although the effect on such in-process parameter control on the microstructure and the texture is relatively well understood, the effect on the distribution of residual stress (RS) still represents a research gap. Since RS may cause premature in-service part failure, RS are an important factor for the structural integrity of parts [15]. Although the required subsequent heat treatments of IN718 can mitigate most of the RS, they cannot prevent thermal stress-induced distortion or cracking prior to post-process heat treatments [16]. In addition, the proposed tailored heat treatments, designed to take advantage of the characteristic microstructure features, are performed at lower temperatures to reduce the thermal effect [17]. Consequently, it remains paramount to understand the RS distribution in as-built IN718 parts and after heat treatment. In this context, RS can be determined by diffraction-based techniques in a non-destructive fashion. In essence, measured lattice plane distances are converted to lattice strain using a stress-free reference. With knowledge of the diffraction elastic constants lattice strains are connected to the macroscopic stress by Hooke's law. In theory, at least six components need to be measured to determine the full RS tensor. However, if the principal stress axes are known the number of required measurements can be reduced to three [18]. In the context of PBF-LB lattice structures, Fritsch et al. [19] have shown that only measurements in nine directions were sufficient to resolve both the principal stress magnitude and directions in a reliable way. In general, the rather complex thermal history induced by the layer-by-layer manufacturing strategy in PBF-LB precludes such an assumption [20]. In consequence, the assessment of the directional RS may still be correct, but they do not represent the principal stress magnitudes [18]. With this in mind, Vrancken [21] has determined, using X-ray diffraction, that the direction of principal stress at the part upper surface is always equal to the direction of the scan vectors in the last manufactured layer. In addition, Bayerlein et al. [20] performed neutron diffraction experiments to determine the RS in Inconel 718 cuboids. In contrast to Vrancken, they report that the principal stress directions in the bulk at a point close to the surface coincide with the sample coordinate system. This apparent discrepancy can be attributed to the characteristics of lab X-ray and neutron diffraction techniques: the sampling volumes are different (i.e., X-ray diffraction is a surface technique and neutron diffraction is a bulk technique).

In the present study, we fabricated vertical IN718 prisms ($13 \times 13 \times 111$ mm^3) by varying the scan strategy along the build height. We characterized the full RS tensor by measuring in thirteen different directions at each point along the height. To obtain spatial information on the microstructure and texture, the RS characterization was complemented by microstructural analysis using electron backscatter diffraction. We aimed to characterize the significance of scan strategy variations on the principal stress directions and magnitudes. Our findings shed further light on the interplay between the microstructure, the texture and the RS in PBF-LB Inconel 718. Our results contribute to the establishment of the metrological robustness of RS measurements by diffraction-based methods.

2. Materials and methods

2.1. Sample manufacturing

Two vertical PBF-LB/M/IN718 prisms with the dimensions $13 \times 13 \times 111$ mm^3 were manufactured using an SLM 280 (SLM Solutions Group AG, Lübeck, Germany) (Fig. 1a). The specimens were manufactured with their longest direction oriented along the build direction (i.e., z // BD). The following laser beam parameters developed by SLM Solutions were applied: scanning velocity $v = 800$ mm s^{-1}, spot size diameter of 0.08 mm defocused by 4 mm, hatch spacing $h = 0.15$ mm, laser power $P = 350$ W, and layer thickness 0.06 mm. In addition, the baseplate was pre-heated to 200 °C. To reduce heat accumulation during production, a longer interlayer time (i.e., time between laser exposure of successive layers) of 81 s was selected (see [22]). To prevent oxidation during manufacturing the build chamber was kept under argon atmosphere with a constant gas flow.

In total three different scan strategies without contour/border varying over the build height were applied. The different scan strategies are depicted in Fig. 1a. In sections 1 and 4, the alternating scan vectors followed the axes of the sample coordinate system with a 90° interlayer rotation. In contrast, in sections 2 and 5 the scan vectors were rotated by 45° with respect to the sample coordinate system while maintaining the 90° interlayer rotation. In section 3 the alternating scan vectors were rotated by 67° between each layer in a continuous manner. After manufacturing, the prisms were cut from the baseplate and were investigated in the as-built condition.

2.2. Electron backscatter diffraction

For microstructural analysis by electron backscatter diffraction (EBSD), longitudinal cross-sections were extracted in the y-z plane (cut at $x \approx 6.5$ mm) along the full height of a sister prism. The metallographic sections were mounted in conductive epoxy resin (Technotherm 3000, Kulzer GmbH, Hanau, Germany) and prepared by grinding using SiC emery papers (P600, P1200, P2500, and P4000). The sections were polished using 3 μm and 1 μm diamond paste for 5 and 10 min respectively. The final polishing step was performed using MasterMet 2 colloidal silica (0.02 μm) suspension for 15 min (Buehler Ltd.,

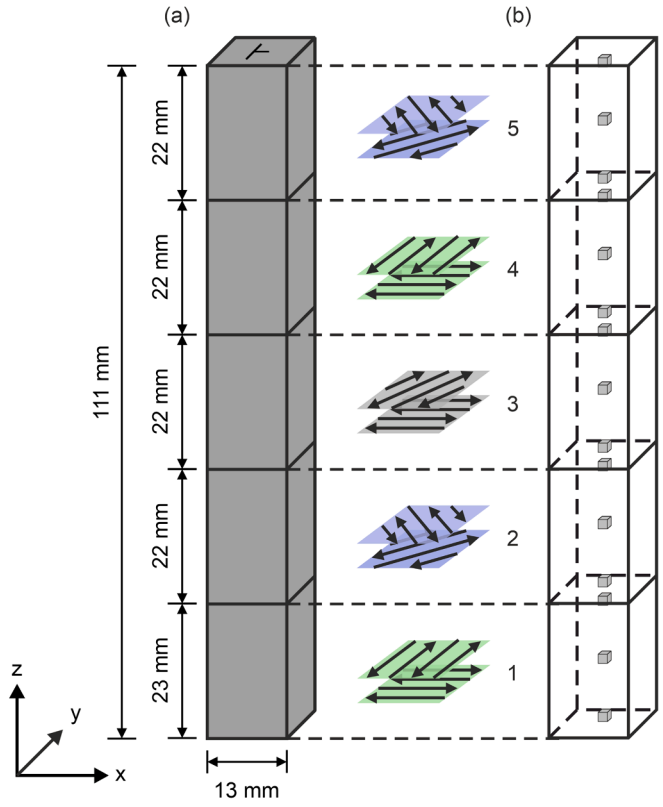

Fig. 1. (a) Sample geometry and scan strategies, (b) neutron diffraction measurement positions.

Leinfelden-Echterdingen, Germany). The microstructural analysis was performed on a TESCAN Vega 3 scanning electron microscope (SEM) (Brno, Czech Republic) equipped with an Oxford Instruments Symmetry S3 EBSD detector (Abingdon, United Kingdom). The SEM was operated at an acceleration voltage of 20 kV, a working distance of 35 mm, and a specimen tilt of 70°. The orientation maps were acquired with a magnification of 100×, a step size of 5 μm, and an exposure time of 3 ms.

For data post-processing the open-source MTEX toolbox [23] within MATLAB (The MathWorks Inc., Natick, USA) was used. The misorientation threshold for calculating high-angle grain boundaries was set to 10°, with only grains containing ≥ 10 pixels included in the analysis. Non-indexed pixels were indexed according to their nearest neighbor. Grain boundary smoothing was performed using the default Kernel function for 25 iterations. Denoising was performed using a variational spline filter [24]. The orientation distribution functions were calculated using a de La Vallée Poussin kernel with a halfwidth of 5°.

2.3. Neutron diffraction

The diffraction measurements were performed at the KOWARI strain scanner located at the Australian Nuclear Science and Technology Organisation (ANSTO). The experimental setup of KOWARI is shown in Fig. 2a. A wavelength of 1.53 Å was selected by the silicon monochromator crystal, Si-400 reflection. This resulted in a diffraction angle $2\theta \approx 90°$ for the selected Ni-311 reflection defining a near cubic gauge volume to ensure that approximately the same set of individual grains are sampled in all measurement directions. The Ni-311 reflection is known to be a good choice for the assessment of macroscopic residual stress in as-built IN718 specimens [12,13,25] because of the nearly isotropic elastic behavior of 311-grains. The slits in the incoming and diffracted beam defined a $1.5 \times 1.5 \times 1.5$ mm^3 gauge volume. Given the approximate grain size (equivalent diameter) of 70 μm, at least 2350 individual grains are contained in the gauge volume. In total 15 points were measured as a function of the sample height (z) at fixed positions x = 6.5 mm and y = 6.5 mm (see Fig. 1b). The points were distributed in the center of each scan strategy section as well as at a distance of 1.5 mm from the interfaces. A total number of 13 directions were measured for each measurement point distributed according to Fig. 2b. The peak positions were derived using a gaussian profile fit and converted to lattice spacings d^{311} using Bragg's law [26]. The stress-free reference lattice spacing (d_0^{311}) was derived from the boundary condition that the out-of-plane component of the top surface must equal zero ($\sigma_{zz} = 0$ at z = 111 mm).

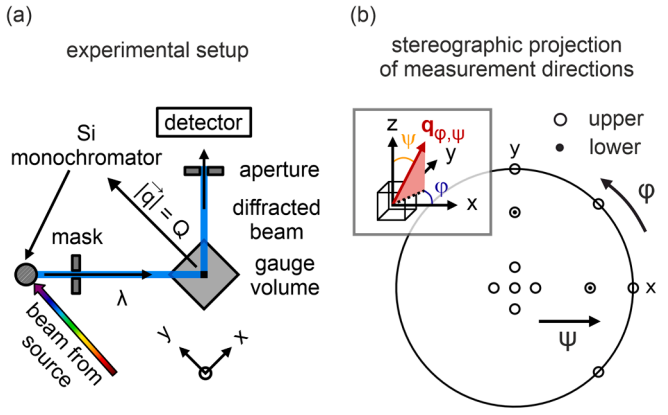

Fig. 2. (a) neutron diffraction setup at KOWARI at $\varphi = 90°$, $\psi = 90°$ reproduced under terms of the CC-BY license [12], (b) stereographic projection of the 13 measurement directions. The small inset shows the relationship of the scattering vector q to the sample coordinate system.

2.4. Residual stress analysis

2.4.1. Determination of the residual stress tensor

For the determination of the six unknown components necessary to uniquely identify the residual stress tensor, Hooke's law can be written in the special form of Dölle & Hauk [27] (equation (1)). In the following it is referred to the least-squares method as proposed by Ortner [28–30]. However, we consider that the elements of the stress factors are entries of the fourth rank elasticity tensor [31]. Therefore, the stress factor entries are denoted as F_{33ij} instead of F_{ij}. In addition, these elements contain the coordinate transformations relating specimen and laboratory frames of reference [31].

$$\langle \varepsilon_{33}{}^{L} \rangle = \langle \varepsilon^{L}_{\varphi\psi} \rangle = \frac{d^{hkl}(\varphi,\psi,311) - d_0^{hkl}(\varphi,\psi,311)}{d_0^{hkl}(\varphi,\psi,311)} = \sum_{ij=1}^{3} F_{33ij}(\varphi,\psi,311)\langle \sigma^{s}_{ij} \rangle \tag{1}$$

Given the symmetry of both **F** and **σ** equation (1) can be written in the Voigt notation (equation (2)) [28]. Therefore, the entries of σ_k and F_{3k} are given by the equations (3) and (4) [28].

$$\langle \varepsilon_{33}{}^{L} \rangle = \langle \varepsilon^{L}_{\varphi\psi} \rangle = \sum_{k=1}^{6} F_{3k}(\varphi,\psi,311)\sigma_k \tag{2}$$

$$\{\sigma_k\} = \{\sigma_{11},\sigma_{22},\sigma_{33},\sigma_{23},\sigma_{13},\sigma_{12}\} \tag{3}$$

$$\{F_{3k}\} = \{F_{3311},F_{3322},F_{3333},2F_{3323},2F_{3313},2F_{3312}\} \tag{4}$$

In case of the 13 measurement directions (n ∈ [1,13]), an overdetermined linear equation system can be formulated for each of the 15 measurement positions in the specimen (equation (5)). Note that each of the stress factor entries still depend on *hkl*, *φ*, and *ψ*. Solving for σ_k, the six unknowns of the residual stress tensor can be determined.

$$\begin{pmatrix} \langle \varepsilon^{L}_{\varphi\psi} \rangle_1 \\ \vdots \\ \langle \varepsilon^{L}_{\varphi\psi} \rangle_n \end{pmatrix} = \begin{pmatrix} F_{311} & F_{321} & F_{331} & F_{341} & F_{351} & F_{361} \\ \vdots & \vdots & \vdots & \vdots & \vdots & \vdots \\ F_{31n} & F_{32n} & F_{33n} & F_{34n} & F_{35n} & F_{36n} \end{pmatrix} \times \begin{pmatrix} \sigma^{s}_1 & \sigma^{s}_2 & \sigma^{s}_3 & \sigma^{s}_4 & \sigma^{s}_5 & \sigma^{s}_6 \end{pmatrix}^{T} \tag{5}$$

The stress factor entities were calculated from the Reuss single-crystal elastic constants refined for PBF-LB/M/IN718 [25] using ISODEC [32]. To account for the crystallographic texture, the orientation distribution functions determined from the EBSD measurements were used for the calculation of the stress factors for each individual measurement position.

2.4.2. Principal stress directions and magnitudes

Rewriting the obtained six components of the residual stress tensor (in the sample reference system) in the second rank tensor form (with $\sigma_{ij} = \sigma_{ji}$), an eigenvalue decomposition can be performed using equation (6).

$$\begin{pmatrix} \sigma_{11} & \sigma_{12} & \sigma_{13} \\ \sigma_{12} & \sigma_{22} & \sigma_{23} \\ \sigma_{13} & \sigma_{23} & \sigma_{33} \end{pmatrix} = (\nu_1,\nu_2,\nu_3) \begin{pmatrix} \sigma_1 & 0 & 0 \\ 0 & \sigma_2 & 0 \\ 0 & 0 & \sigma_3 \end{pmatrix} \times (\nu_1,\nu_2,\nu_3)^{-1} \tag{6}$$

The results are the three eigenvectors $\mathbf{v_1}$, $\mathbf{v_2}$, $\mathbf{v_3}$ (i.e., the principal stress directions) and their associated eigenvalues σ_1, σ_2, σ_3 (i.e., the principal stress magnitudes).

2.4.3. Implementation

The procedure was implemented in a Python script using a Monte-Carlo approach to account for measurement uncertainties in the obtained eigenvalues and eigenvectors. The workflow is shown in Fig. 3.

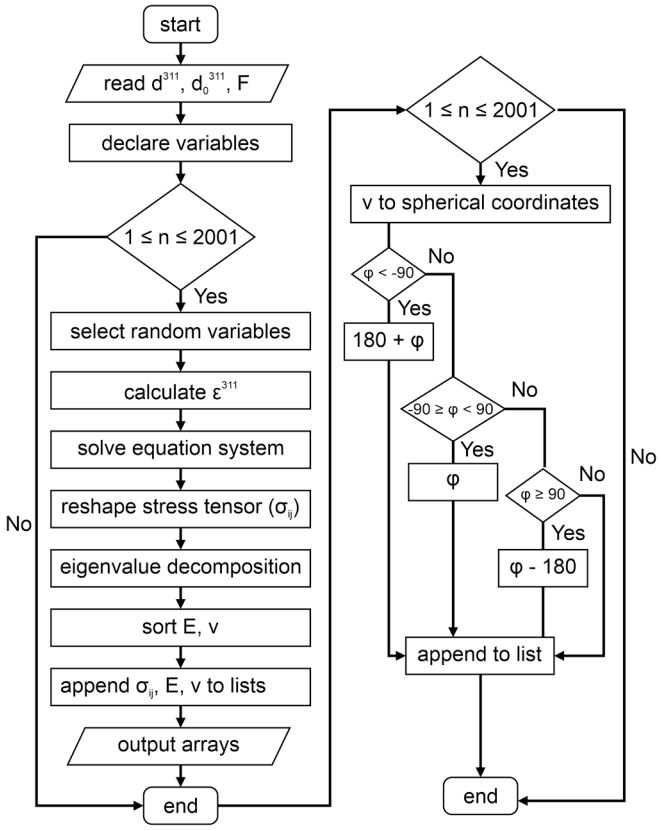

Fig. 3. Workflow to determine the principal stress magnitudes and directions. Random variables are generated from the determined lattice distances from which the solution of the linear equation system (eqn. (5)) is used to perform an eigenvalue decomposition (eqn. (6)). The eigenvalues and eigenvectors are sorted and transformed considering their symmetry.

3. Results and discussion

3.1. Microstructure & texture

3.1.1. Impact of scan strategies

The orientation maps recorded at the 5 different sections corresponding to the different scan strategies are shown in Fig. 4a-e. This analysis shows how the microstructure and the texture change across the build height for these different scan strategies. In addition, the spatial information of the microstructure and the texture helps us to account for the variation in crystallographic texture for the determination of the residual stress. Overall, the grain size is insensitive to the build height and only slightly sensitive to changes of the scan strategy (Fig. 4a-i). Such observation highlights the absence of significant heat accumulation during processing since heat accumulation would lead to a noticeable increase of the grain size [22]. In view of the grain morphology, it is common to observe heterogeneous but periodic grain structures with two alternating characteristic microstructural regions in PBF-LB Inconel 718 for 90° interlayer rotation [33]. Sonntag et al. [33] classified the regions as having either a predominant elongated grain morphology or as columns of stacked grains with a ripple pattern. Other authors just classify these characteristic microstructures as bimodal [34,35]. In fact, we observe such microstructure characteristics for both scan strategies possessing an interlayer rotation of 90° (Fig. 4a, d and Fig. 4b, e). However, we find that the variation of the scan strategy resulted in significant changes of the crystallographic texture when applying 90° interlayer rotation. While the scan strategy does not influence the crystallographic texture along the build direction, it controls the orientation of the crystals in the build plane (i.e., xy-plane) (Fig. 5) [34]. In fact, when the scan vectors are parallel to the x- and y- axes of the sample coordinate system (i.e., section 1 and 4), the faces of the fcc crystals point in these directions (i.e., have a ⟨1 0 0⟩-type texture) (see Fig. 4b, e and Fig. 5). In contrast, the rotation of the scan vectors by 45° leads to a correspondent rotation of the fcc crystals. In effect, the edges of the cubic crystals are parallel to the x- and y- axes of the sample coordinate system (i.e., ⟨1 1 0⟩/⟨1 1 1⟩-type texture) (see Fig. 4a, d and Fig. 5). These observations are in line with previous studies applying similar scan strategies with an interlayer rotation of 90° to produce PBF-LB IN718 [9,13,34]. When we apply a continuous rotation of the scan vectors by 67° between each layer (section 3 in Fig. 1), we obtain a nearly random orientation of the crystals (see Fig. 4c and Fig. 5). Besides the absence of crystallographic texture, the layer-by-layer change of the heat flow direction caused by the continuous interlayer rotation promotes changes in the grain morphology. Compared to the scan strategies applying an interlayer rotation of 90°, we observe that the grains lose their characteristic shape. In this context, several authors applying scan strategies with a continuous interlayer rotation of 67° also observed such changes in grain morphology characteristics [35–38]. In addition, other researchers observed that texture intensities were reduced but some preferred alignment with ⟨1 0 0⟩ parallel to the build direction remained [35,37,38]. As we already discussed in [13] the microstructure of PBF-LB/IN718 depends on many different processing parameters affecting the solidification conditions. This fact prevents a general conclusion.

3.1.2. Microstructure evolution at interfaces

In view of the interfaces between the sample sections with different scan strategies, we observe that the response of the material to the change of the scan strategy is characteristic to each transition. The transition zones can be identified in the orientation-maps Fig. 4f-i. The calculation of the mean Euler angles with respect to the build direction enables the quantification of these transition zones (Fig. 4f.1-i.1). It becomes clear that the change of orientation is more pronounced at the interfaces of section 1 → 2 and 4 → 5, whereas it is less distinct for the interfaces of section 2 → 3 and 3 → 4. This links to the underlying scan strategy since section 3 (i.e. 67° rotation) shows no preferred grain orientation. Therefore, the misorientation to the adjacent sections is smaller compared to the transition from the sections with 90° interlayer rotation. In fact, the transition from section 2 → 3 occurs over 600 μm (Fig. 4h.1). At the other interfaces, the microstructure transition zone has a thickness ranging from 100 to 200 μm (Fig. 4f.1, g.1, i.1). Thus, altering the scan strategy offers an elegant tool to design the crystallographic texture in a material without changing the grain arrangement. This can be achieved by changing the orientation of the scanning pattern with respect to the sample coordinate system. Another approach to tailor the microstructure and the texture is provided by alteration of the laser beam parameters. For instance, Niendorf et al. [39,40] showed for PBF-LB/316L that the microstructure and the texture can be controlled using different laser powers. On the one hand, a fine-grained microstructure with [0 0 1]/[1 1 0] texture along the build direction forms using a 400 W laser. On the other hand, a columnar-grained coarse microstructure with a dominant [0 0 1] texture along the build direction forms using a 1000 W laser. The authors explain the formation of such characteristic microstructure by the fact that the direction of heat flow dictates the texture evolution. Since the energy input becomes large using a 1000 W laser, the corresponding melt pools are large and thus lower temperature gradients develop [40]. Hence, the local variations are not as pronounced compared to using a 400 W laser, and epitaxial growth occurs [40]. Even though Niendorf et al. [39] altered the laser power instead of the scan strategy, they also observed a sharp microstructure transition. Popovich et al. [14] later showed, using a similar approach (250 W and 950 W zones), that the microstructure and the texture formation in PBF-LB/IN718 is similar to the work of Niendorf et al.. Therefore, PBF-LB enables the production of graded microstructures in two different ways. First, the alteration of the laser beam parameters (e.g., laser power

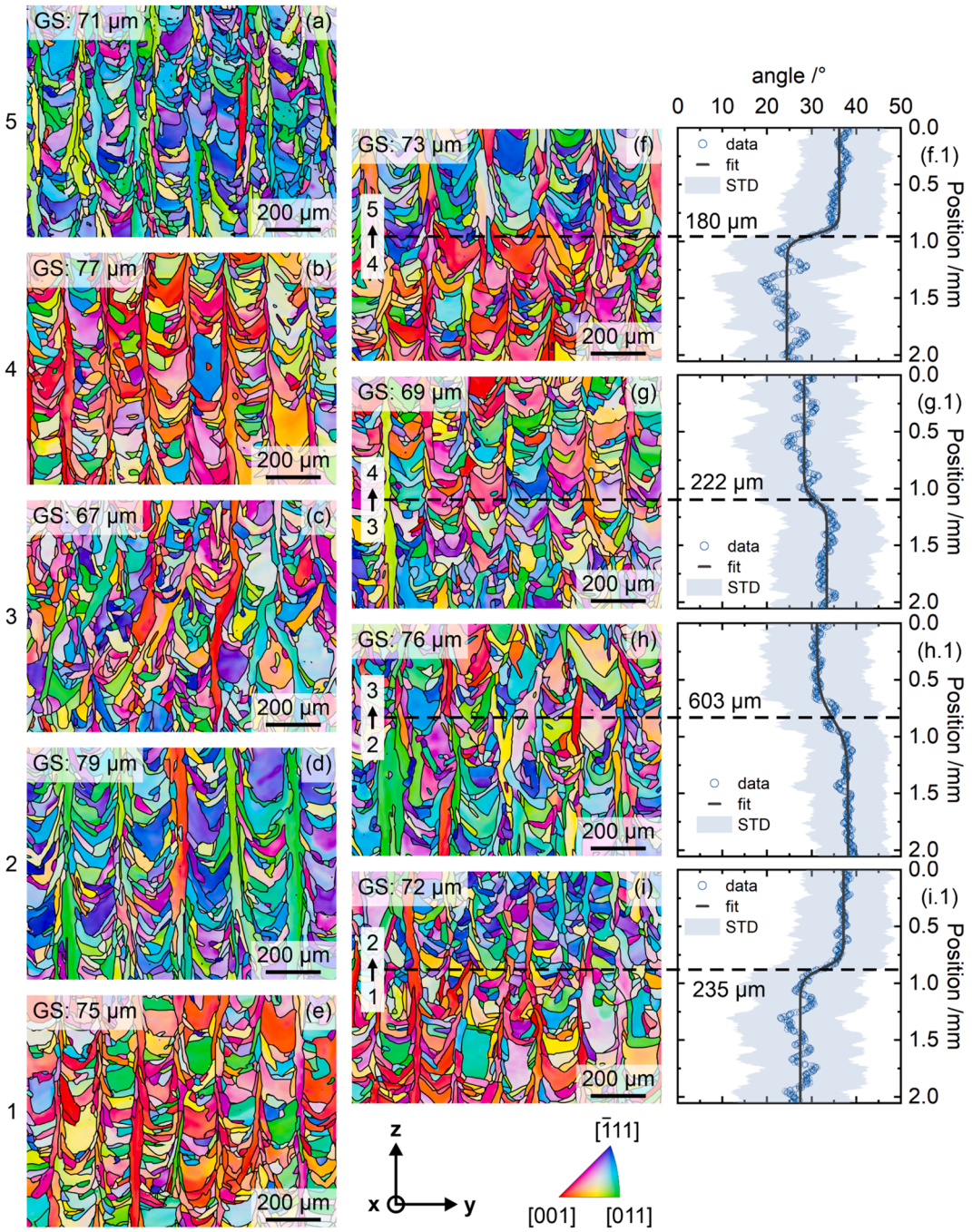

Fig. 4. Orientation maps of the different scan strategies in the middle of sections 1 to 5 (a-e) and at the interfaces of each section (f-i) viewed along x. GS denotes the average of the equivalent spherical diameter weighted by the area fraction with a standard deviation of about 43 µm. Characterization of the microstructure interface using the y-average of the second euler angle plotted along z (f.1-i.1).

and speed) enables the control of both, the texture, and the grain morphology. Second, the alteration of the scan strategy enables the control of the crystallographic texture perpendicular to the build direction with minor impact on the solidification conditions.

3.2. Residual stress

3.2.1. Components of the RS tensor

In Fig. 6a-d, the determined six components of the residual stress tensor (in the sample coordinate system) are shown as a function of the sample height z. This enables us to understand the impact of different scan strategies on the RS distribution. The horizontal dashed lines correspond to the interfaces between different scan strategies, whereas the horizontal solid lines correspond to the top and the bottom of the specimen. The numbers represent the labels of each section according to Fig. 1a. In Fig. 6a, the RS components along the axes of the sample coordinate system axes are shown. The components $\sigma_{xx} \approx -125$ MPa and $\sigma_{yy} \approx -100$ MPa are of smaller magnitude compared to the stress component along the build direction (i.e., $\sigma_{zz} \approx -700$ MPa). Overall, no significant RS gradient is observed with respect to the build height (i.e., z coordinate). Furthermore, the RS magnitudes in sections manufactured with equivalent scan strategies are similar. Hence, the influence of the build height on the RS is minimal. At the top of the sample, we observe a plane stress condition; σ_{xx} and σ_{yy} become tensile. We must

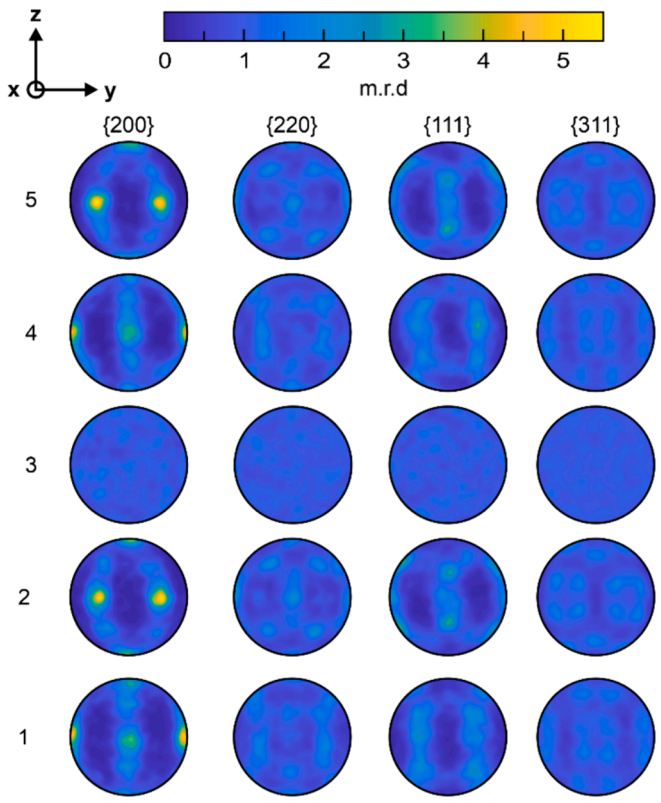

Fig. 5. {200}, {220}, {111}, {311} pole figures extracted from the calculated orientation distribution functions of the middle of sections 1-5.

note that the center of the gauge volume at the bottom is positioned 2.4 mm away from the surface, so that $\sigma_{zz} \neq 0$. In fact, we observed in one of our previous studies that the top surface of PBF-LB/IN718 prisms, manufactured in horizontal orientation, exhibit tensile RS in the two in-plane directions [12]. This observation agrees with other studies conducted by several authors [20,37,41]. In view of the different scan strategies, the values of σ_{xx} and σ_{yy} depend on the measurement position. Where the scan vectors align with the x- and y- axes of the sample coordinate system (i.e., sections 1 and 4), the difference between σ_{xx} and σ_{yy} becomes maximal. Compared to such scan strategy, the difference between σ_{xx} and σ_{yy} are smaller when the scan vectors are rotated by 45° to the geometry, even maintaining the 90° interlayer rotation (i.e., sections 2 and 5). Again, this observation agrees well with our previous studies on horizontally manufactured specimens produced with similar scan strategies [12]. With application of a continuous scan vector rotation by 67° between each layer the stress state becomes transverse isotropic (i.e., $\sigma_{xx} \approx \sigma_{yy}$ in section 3). In fact, the in-plane shear stress shown in Fig. 6b reflects this situation: $\sigma_{xy} \approx 0$ in sections 1 and 4, while σ_{xy} is non-zero in sections 2, 3, and 5, where the in-plane stress is more isotropic. The out-of-plane shear components σ_{xz} (Fig. 6c) and σ_{yz} (Fig. 6d) show no clear trend with the sample height z. Overall, we must note that the shear components are of low magnitude (see Fig. 6b-d). As a final remark, a comparison to other studies remains difficult due to several reasons. First, the geometry of the specimens affects the residual stress distributions (and in particular, the dominant stress component) in the specimens. Second, the choice of the boundary condition for the determination of the stress-free reference does not consider spatial variations along the specimen height. In general, the latter aspect is not a concern for PBF-LB specimens built with uniform manufacturing strategies [12,41,42]. However, in our case the changes of the scan strategy with respect to the sample height might cause such spatial gradients. In fact, we observed in a previous study that the stress-free references of different scan strategies differed from each other [12]. Such a study of d_0 gradients was out of scope of this work, since while the stress-free reference might affect the absolute magnitude of residual stress at different measurement positions, it does not change the relation among the principal stress magnitudes and should have a minor influence on the principal directions.

3.2.2. *Scan strategies determine the principal stress directions*

The results of the eigenvalue decomposition calculations based on Monte-Carlo simulations are shown as stereographic projections in the x-y plane in Fig. 7. The points are colored according to their principal stress magnitude. The points are drawn at positions in the projection corresponding to the eigenvector direction. Irrespective of the scan strategy, the largest bulk RS magnitude aligns with the z direction (i.e., build direction). This can be related to the fact that the laser beam parameters control most of the thermal gradient along the build height. Since we did not alter the laser beam parameters, the principal stress direction angle with respect to z does not change. Moreover, the shrinkage of molten layers during cooling adds additional stress to those layers that are influenced by the temperature gradient mechanism [7].

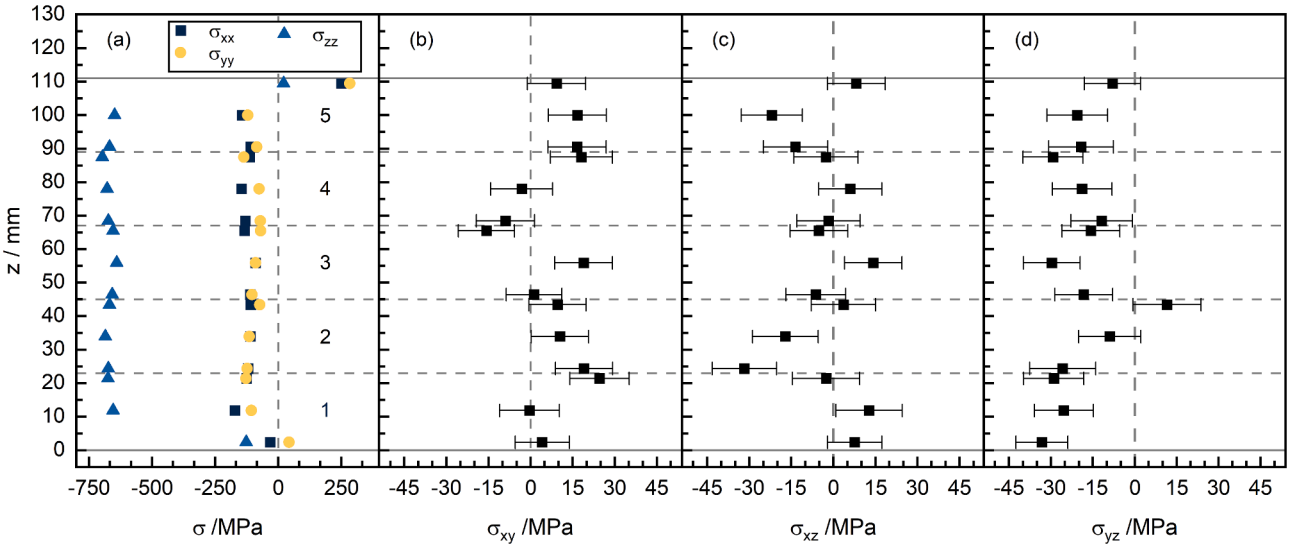

Fig. 6. Mean components of the residual stress tensor components as determined by the solution of the linear equation system as a function of the sample height z. (a) σ_{xx}, σ_{yy}, σ_{zz}, (b) σ_{xy}, (c) σ_{xz}, and (d) σ_{yz}. In (a) errors are within the size of the symbols.

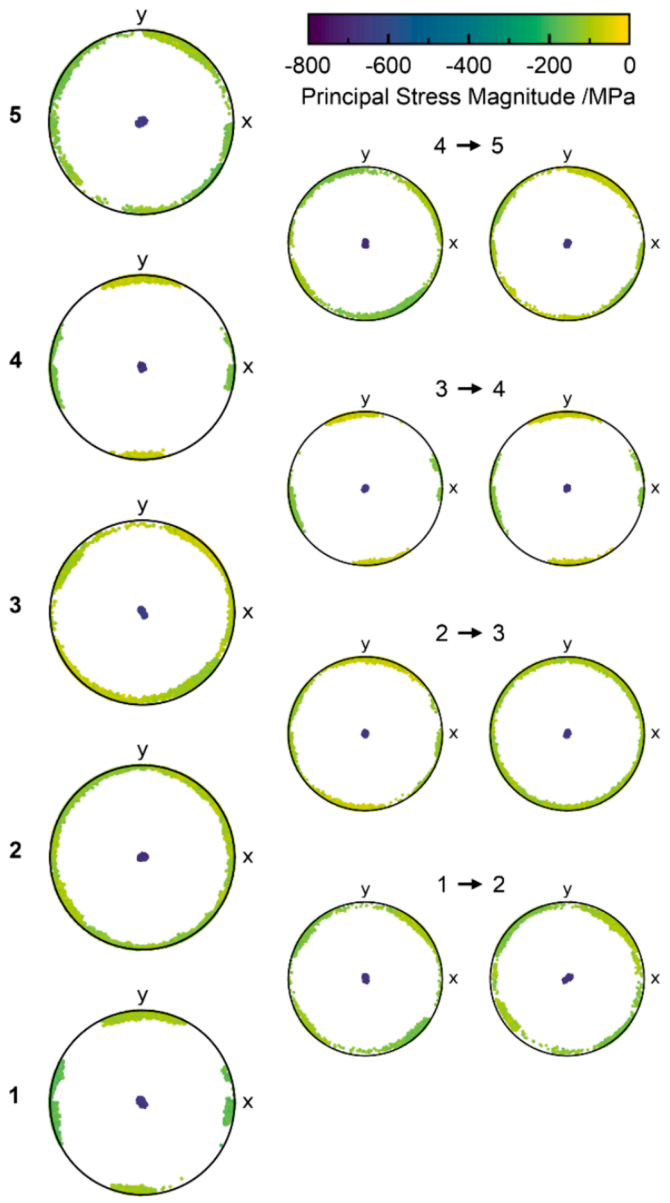

Fig. 7. Stereographic projections of the principal stress directions colored according to their principal stress magnitudes. Sections 1 and 4 display a clear alignment of the principal axes with x, y, z, whereas in the other cases the stress is nearly in-plane isotropic in the build plane.

Therefore, the shape of the manufactured geometry has a profound effect on the formation of the shrinkage stresses and thus on the final RS distribution. Even further, Schmeiser et al. [43] have shown by in-situ synchrotron X-ray diffraction during PBF-LB of IN625, that the strain evolution at a fixed position depends on the number of layers manufactured above the investigated position (i.e., on the total build height).

As the analysis of the stress tensor components already suggests, we observe different distributions of the principal stress within the x-y plane. Whenever the scan vectors are parallel to the x- and y- axes of the sample coordinate system (i.e., sections 1, 4), the principal stress directions align with them. In such a case the larger in-plane RS magnitude corresponds to the x-direction, whereas the smallest magnitude is found with the y-direction (i.e., $\sigma_{zz} \approx \sigma_3 < \sigma_{xx} \approx \sigma_2 < \sigma_{yy} \approx \sigma_1 < 0$). For the situation where the scan vectors are rotated by 45° to the x- and y- axes of the sample coordinate system (sections 2, 5), we observe a clustering (of Monte-Carlo generated measurement points) at an approximate angle of 45° between x and y. The fact that $\sigma_{xx} \approx \sigma_{yy}$ at these positions and that the shear stresses are of small magnitude result in the principal stress directions to be undefined [30,44]. In fact, a similar situation holds true in section 3. In contrast to the microstructure transitions at the section boundaries, we find a rather smooth transition of the residual stress state close to the interfaces. In the manufactured layer itself, the in-plane thermal gradient changes immediately in response to the scan strategy. In contrast, due to remelting and reheating, the change in thermal gradient in the underlying layers occurs over a greater length of time. In fact, once the underlying layers are no longer affected by remelting, the microstructure formed is stable due to the avoidance of further heat accumulation. This explains the rather sharp microstructure transitions. However, the underlying layers are still exposed to temperatures affecting the thermal stress and thus the final RS distribution and associated gradients (see [43]). Therefore, since the thermal stress state above the interface affects the thermal history below it, we observe a rather continuous rotation of the in-plane RS components (e.g., 3 → 4 in Fig. 7).

With the knowledge of the symmetry of the residual stress distribution (i.e., −x and x point in the same direction), we can run a statistical analysis of the principal stress directions. In Fig. 8 such results are shown for the azimuthal angles φ_1 and φ_2 associated to the in-plane principal stress σ_1 and σ_2. The third principal direction is invariant to the azimuthal angle φ_3, since the out-of-plane principal component always points in the direction $\psi_3 = 0°$. The same argument holds true for ψ_1 and ψ_2 as they describe directions lying in the x-y plane, hence they have a value of 90° (see Fig. 2b). Therefore, only the statistics of φ_1 and φ_2 are required to describe the effect of the scan strategy on the distribution of the principal stress directions. First, the mean values of φ_1 and φ_2 correspond well to the scan strategy used. Second, whenever the measurement position is close to an interface, the mean value lies between the point measured below and above that interface. However, we observe a larger mismatch of the principal stress direction at the interface between section 4 and 5. Third, the spread of the distribution highlights the scatter of the principal stress direction angle. By quantification we find mean and standard deviations of $\varphi_1 = 91° \pm 9°$ and $\varphi_2 = 0.1° \pm 9°$ corresponding to scan strategies following the x and y axes of the sample coordinate system (Fig. 8 sections 1 and 4). When the scan vectors are rotated by 45° to the x and y axes of the sample coordinate system, these values change to $\varphi_1 = 63° \pm 15°$ and $\varphi_2 = -27° \pm 15°$. In the most extreme case (i.e., 67° continuous interlayer rotation), no dominant direction of the principal stress exists in the x-y plane at the interface between sections 2 and 3. Therefore, it can be concluded that in such a case the distribution of the principal stress directions possess a transverse isotropy (see also Fig. 6). To study the RS formation during PBF-LB of Ti64, Zhang et al. [45] have combined experiments with finite element modeling. They found that even a 90° interlayer rotation can significantly reduce the directionality of the in-plane RS compared to no interlayer rotation. This highlights the importance of the cumulative difference in the temperature field during production. As mentioned above, such an observation is also related to microstructure formation, since the temperature gradient also affects solidification and grain growth (Fig. 4). Therefore, we must emphasize that in addition to the scan vector orientation, the interlayer rotation influences both the microstructure and the RS formation. Furthermore, the above statements are rigorously valid only for the sample central axis, while for other points within the sample the situation could be different.

3.2.3. Errors induced by measuring along the three orthogonal axes of the sample coordinate system

Due to time constraints, it is often necessary to measure as few directions as possible when conducting neutron diffraction experiments. Therefore, the typical approach is to measure along three orthogonal directions, most often the axes of the sample coordinate system. It is instructive to study the difference between the principal stress magnitudes (σ_1, σ_2, and σ_3) and the stress components determined in three orthogonal directions corresponding to the axes of the sample

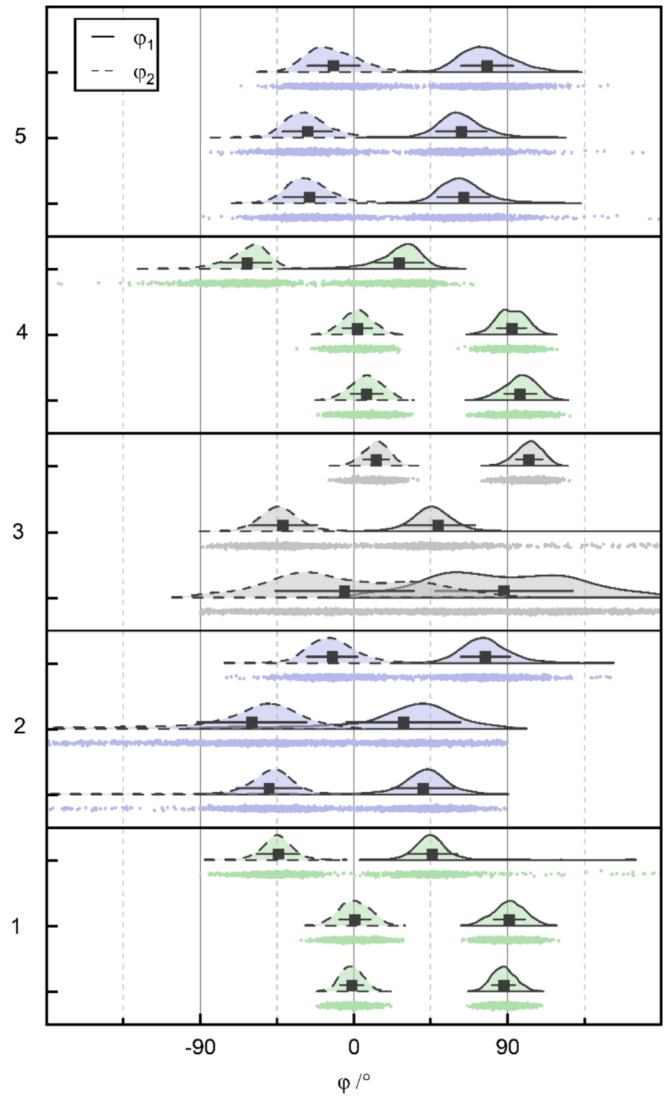

Fig. 8. Distributions and mean values of the two principal angles φ_1 and φ_2 along the build height considering the symmetry of the principal stress directions (i.e., −x equal to x). The colored points correspond to each single Monte-Carlo calculation, while the distributions depicted above the point clouds show the frequency and the spread of the values.

coordinate system (σ_{xx}, σ_{yy}, and σ_{zz}). Even though the material in this study shows some crystallographic texture, its influence on the RS has been shown to be insignificant [12]. Fig. 9a shows the mean of the principal stress magnitudes as a function of the specimen height. Such values can be compared with the corresponding σ_{xx}, σ_{yy}, and σ_{zz}. The corresponding differences are plotted in Fig. 9b. Statistical errors increase when measurements are just performed along three orthogonal directions. We observe that the stress difference between the principal stress and the directional RS approaches 0 whenever the scan strategy aligns with the x- and y- axes of the sample coordinate system (i.e., sections 1 and 4). For the other positions, the stress difference between the in-plane components (σ_2-σ_{xx} and σ_1-σ_{yy}) increases. This is because the principal stress direction does not coincide with the sample coordinate system. The largest stress difference is observed at the interface of section 4 → 5 and 1 → 2, while they are insignificant at the interface 2 → 3 and 3 → 4. This finding correlates well with the microstructure transition as seen in Fig. 4f.1-i.1. We can speculate that the RS gradient at the interfaces is driven by the "strength" of the microstructure transition. This would explain the larger stress difference at interfaces characterized by a more pronounced change in grain orientation. In any case, one

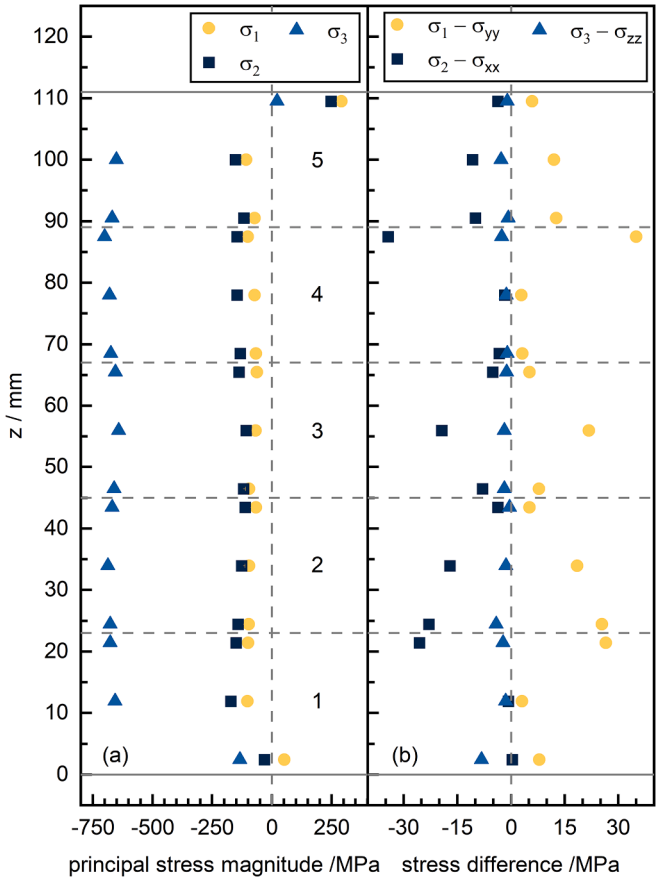

Fig. 9. (a) Average principal stress magnitude as a function of the sample height z. The errors are within the symbol size. (b) Stress difference between the directional stress and the three associated principal stress magnitudes.

can note that that the maximum of the stress difference does not exceed 30 MPa, which is in the range of typical uncertainties in neutron diffraction RS measurements [46]. Thus, for the specific geometry, in the specimen central axis, measuring the three orthogonal directions corresponding to the sample coordinate system can be considered sufficient to fully characterize the RS state. Fritsch et al. [19] have shown that for PBF-LB/IN625 lattice structures nine directions were required to characterize the RS state. Even though in theory six directions are sufficient to characterize all components of the RS tensor, the required number of measurement directions tends to be dependent on the part complexity [19].

4. Conclusions

In this work, we investigate the influence of the scan strategy on the residual stress in a graded Inconel 718 rectangular prism with a square cross-section. Different crystallographic textures were obtained by in-process variation of the scan strategy during laser powder bed fusion. The effects of the in-process change of the scan strategy on the microstructure and on the residual stress were discussed. From this work, the following conclusions can be drawn:

- Microstructural analysis using electron backscatter diffraction revealed sharp microstructural transitions between regions produced by different scan strategies. The interface regions extend over 100–200 μm.
- The dominant principal stress magnitude in the bulk is found to be ≈ 700 MPa in compression along the largest dimension (i.e., the building direction). The other two principal stress components are

smaller in magnitude by a factor of 6. In contrast to the microstructure, neutron diffraction measurements showed that jumps in the residual stress tensor, measured and evaluated along the central line, occur in a more gradual manner.

- Altering the scan strategy leads to some misorientation of the principal axis of the stress tensor in the build plane with the following three scenarios:
  (1) Whenever the scan vectors align with the sample coordinate system, the principal stress directions co-align.
  (2) A 45° rotation of the scan vectors with respect to the geometry causes a 30° deviation of the principal directions from the geometric axes. However, the difference between the principal stress magnitudes and the stresses along the axes of the sample coordinate system does not exceed 30 MPa.
  (3) A transversely isotropic stress state develops for a continuous 67° interlayer rotation. This is associated with changing the in-plane thermal gradient after each manufactured layer.

Overall, the findings of this study reveal a small but measurable effect of the scan strategy on the residual stress main axis rotation. The absolute differences between the residual stress measured along the axes of the sample coordinate system and the principal stress directions remain on a low level of 30 MPa. Therefore, in the center of such simple geometries, we propose that measurements along the three axes of the sample coordinate system are sufficient to reliably determine the residual stress state of the specimen. For more complex parts we recommend to account for the scan strategy for part production. In addition, it is recommended to adapt the measurement procedure to the complexity of the part (i.e., by increasing the number of measurement directions).

CRediT authorship contribution statement

Jakob Schröder: Writing – review & editing, Writing – original draft, Visualization, Software, Project administration, Investigation, Formal analysis, Conceptualization. **Tobias Fritsch:** Writing – review & editing, Writing – original draft, Visualization, Software. **Vladimir Luzin:** Writing – review & editing, Methodology, Investigation, Formal analysis. **Bruno Ferrari:** Writing – review & editing, Writing – original draft, Investigation. **Juan Simón-Muzás:** Writing – review & editing, Investigation. **Alexander Evans:** Writing – review & editing, Supervision, Conceptualization. **Giovanni Bruno:** Writing – review & editing, Supervision, Resources.

Declaration of competing interest

The authors declare that they have no known competing financial interests or personal relationships that could have appeared to influence the work reported in this paper.

Data availability

The raw/processed data required to reproduce these findings cannot be shared at this time due to technical or time limitations. Data will be made available upon reasonable request from the corresponding author.

Acknowledgements

The authors would like to acknowledge Keerthana Chand for help in developing the python script of the Monte-Carlo simulations. We acknowledge Jesper Schröder for the valuable discussion on the eigenvalue decomposition. Finally, we acknowledge the Australian Nuclear Science and Technology Organisation for the provision of neutron beamtime at the KOWARI instrument.

References

[1] M. Attaran, Bus. Horiz. 60 (5) (2017) 677–688, https://doi.org/10.1016/j.bushor.2017.05.011.
[2] A.H. Alami, A. Ghani Olabi, A. Alashkar, S. Alasad, H. Aljaghoub, H. Rezk, M. A. Abdelkareem, Ain Shams Eng. J. 14 (11) (2023), https://doi.org/10.1016/j.asej.2023.102516.
[3] A. Lingenfelter, Welding of inconel alloy 718: A historical overview, superalloy 718 metallurgy and applications, The Minerals, Metals & Materials Society (TMS) (1989) 673–683.
[4] J.P. Collier, H.W. Song, J.C. Phillips, J.K. Tien, Metall Trans A 19 (7) (1988) 1657–1666, https://doi.org/10.1007/Bf02645133.
[5] G.M. Volpato, U. Tetzlaff, M.C. Fredel, Additive Manufacturing (2022) 55, https://doi.org/10.1016/j.addma.2022.102871.
[6] R. Cozar, A. Pineau, Met. Trans. 4 (1) (1973) 47–59, https://doi.org/10.1007/bf02649604.
[7] J.P. Kruth, L. Froyen, J. Van Vaerenbergh, P. Mercelis, M. Rombouts, B. Lauwers, J. Mater. Process. Technol. 149 (1–3) (2004) 616–622, https://doi.org/10.1016/j.jmatprotec.2003.11.051.
[8] P. Mercelis, J.P. Kruth, Rapid Prototyp. J. 12 (5) (2006) 254–265, https://doi.org/10.1108/13552540610707013.
[9] V.V. Rielli, A. Piglione, M.-S. Pham, S. Primig, Addit. Manuf. (2022) 50, https://doi.org/10.1016/j.addma.2021.102540.
[10] O. Gokcekaya, T. Ishimoto, S. Hibino, J. Yasutomi, T. Narushima, T. Nakano, Acta Mater. (2021) 212, https://doi.org/10.1016/j.actamat.2021.116876.
[11] B. Chalmers, Principles of Solidification, in: W. Low, M. Schieber (Eds.), Applied Solid State Physics, Springer, US, Boston, MA, 1970, pp. 161–170, https://doi.org/10.1007/978-1-4684-1854-5_5.
[12] J. Schröder, A. Evans, V. Luzin, G. Abreu Faria, S. Degener, E. Polatidis, J. Čapek, A. Kromm, G. Dovzhenko, G. Bruno, J. Appl. Crystallogr. 56 (Pt 4) (2023) 1076–1090, https://doi.org/10.1107/S1600576723004855.
[13] J. Schröder, A. Evans, E. Polatidis, J. Čapek, G. Mohr, I. Serrano-Munoz, G. Bruno, J. Mater. Sci. 57 (31) (2022) 15036–15058, https://doi.org/10.1007/s10853-022-07499-9.
[14] V.A. Popovich, E.V. Borisov, A.A. Popovich, V.S. Sufiiarov, D.V. Masaylo, L. Alzina, Mater. Des. 114 (2017) 441–449.
[15] M. Gorelik, International Journal of Fatigue 94 (2017) 168–177, https://doi.org/10.1016/j.ijfatigue.2016.07.005.
[16] L. Mugwagwa, I. Yadroitsava, N.W. Makoana, I. Yadroitsev, 9 - Residual stress in laser powder bed fusion, in: I. Yadroitsev, I. Yadroitsava, A. du Plessis, E. MacDonald (Eds.), Fundamentals of Laser Powder Bed Fusion of Metals, Elsevier, 2021, pp. 245–276.
[17] T.G. Gallmeyer, S. Moorthy, B.B. Kappes, M.J. Mills, B. Amin-Ahmadi, A. P. Stebner, Additive Manufacturing (2020) 31, https://doi.org/10.1016/j.addma.2019.100977.
[18] R.A. Winholtz, A.D. Krawitz, Materials Science and Engineering: A 205 (1–2) (1996) 257–258, https://doi.org/10.1016/0921-5093(95)10040-7.
[19] T. Fritsch, M. Sprengel, A. Evans, L. Farahbod-Sternahl, R. Saliwan-Neumann, M. Hofmann, G. Bruno, J. Appl. Crystallogr. 54 (Pt 1) (2021) 228–236, https://doi.org/10.1107/S1600576720015344.
[20] F. Bayerlein, F. Bodensteiner, C. Zeller, M. Hofmann, M.F. Zaeh, Addit. Manuf. 24 (2018) 587–594, https://doi.org/10.1016/j.addma.2018.10.024.
[21] B. Vrancken, Study of Residual Stresses in Selective Laser Melting, 2016.
[22] G. Mohr, K. Sommer, T. Knobloch, S.J. Altenburg, S. Recknagel, D. Bettge, K. Hilgenberg, Metals 11 (2021) 7, https://doi.org/10.3390/met11071063.
[23] F. Bachmann, R. Hielscher, H. Schaeben, Ultramicroscopy 111 (12) (2011) 1720–1733, https://doi.org/10.1016/j.ultramic.2011.08.002.
[24] R. Hielscher, C.B. Silbermann, E. Schmidl, J. Ihlemann, J. Appl. Cryst. 52 (5) (2019) 984–996, https://doi.org/10.1107/s1600576719009075.
[25] J. Schröder, A. Heldmann, M. Hofmann, A. Evans, W. Petry, G. Bruno, Mater. Lett. (2023) 353, https://doi.org/10.1016/j.matlet.2023.135305.
[26] H. Bragg, W.L. Bragg, Proc. R. Soc. Lond. 88 (605) (1913) 428–438, https://doi.org/10.1098/rspa.1913.0040.
[27] H. Dölle, V. Hauk, Int. J. Mater. Res. 69 (6) (1978) 410–417, https://doi.org/10.1515/ijmr-1978-690609.
[28] B. Ortner, Powder Diffr. 24 (S1) (2012) 16–21, https://doi.org/10.1154/1.3139048.
[29] B. Ortner, Mater. Sci. Forum 681 (2011) 7–12, https://doi.org/10.4028/www.scientific.net/MSF.681.7.
[30] B. Ortner, Adv. Mater. Res. 996 (2014) 215–220, https://doi.org/10.4028/www.scientific.net/AMR.996.215.
[31] U. Welzel, E.J. Mittemeijer, J. Appl. Phys. 93 (11) (2003) 9001–9011, https://doi.org/10.1063/1.1569662.
[32] T. Gnäupel-Herold, J. Appl. Crystallogr. 45 (3) (2012) 573–574, https://doi.org/10.1107/s0021889812014252.
[33] N. Sonntag, B. Piesker, L.A. Ávila Calderón, G. Mohr, B. Rehmer, L.A. Jácome, K. Hilgenberg, A. Evans, B. Skrotzki, Advanced Engineering Materials (2024), https://doi.org/10.1002/adem.202302122.
[34] H.Y. Wan, Z.J. Zhou, C.P. Li, G.F. Chen, G.P. Zhang, Journal of Materials Science & Technology 34 (10) (2018) 1799–1804, https://doi.org/10.1016/j.jmst.2018.02.002.
[35] M. Calandri, S. Yin, B. Aldwell, F. Calignano, R. Lupoi, D. Ugues, Materials (basel) 12 (2019) 8, https://doi.org/10.3390/ma12081293.
[36] C. Pei, D. Shi, H. Yuan, H. Li, Materials Science and Engineering: A 759 (2019) 278–287, https://doi.org/10.1016/j.msea.2019.05.007.

[37] I. Serrano-Munoz, A. Ulbricht, T. Fritsch, T. Mishurova, A. Kromm, M. Hofmann, R. C. Wimpory, A. Evans, G. Bruno, Advanced Engineering Materials 23 (2021) 7, https://doi.org/10.1002/adem.202100158.
[38] D. Deng, R.L. Peng, H. Brodin, J. Moverare, Materials Science and Engineering: A 713 (2018) 294–306, https://doi.org/10.1016/j.msea.2017.12.043.
[39] T. Niendorf, S. Leuders, A. Riemer, F. Brenne, T. Tröster, H.A. Richard, D. Schwarze, Advanced Engineering Materials 16 (7) (2014) 857–861, https://doi.org/10.1002/adem.201300579.
[40] T. Niendorf, S. Leuders, A. Riemer, H.A. Richard, T. Tröster, D. Schwarze, Metallurgical and Materials Transactions B 44 (4) (2013) 794–796, https://doi.org/10.1007/s11663-013-9875-z.
[41] P. Pant, S. Proper, V. Luzin, S. Sjöström, K. Simonsson, J. Moverare, S. Hosseini, V. Pacheco, R.L. Peng, Additive Manufacturing (2020) 36, https://doi.org/10.1016/j.addma.2020.101501.
[42] L.M. Sochalski-Kolbus, E.A. Payzant, P.A. Cornwell, T.R. Watkins, S.S. Babu, R. R. Dehoff, M. Lorenz, O. Ovchinnikova, C. Duty, Metallurgical and Materials Transactions A 46 (3) (2015) 1419–1432, https://doi.org/10.1007/s11661-014-2722-2.
[43] F. Schmeiser, E. Krohmer, N. Schell, E. Uhlmann, W. Reimers, Additive Manufacturing (2020) 32, https://doi.org/10.1016/j.addma.2019.101028.
[44] D.A. Witte, R.A. Winholtz, S.P. Neal, Advances in X-Ray Analysis 37 (2019) 265–278, https://doi.org/10.1154/s0376030800015779.
[45] W. Zhang, D. Guo, L. Wang, C.M. Davies, W. Mirihanage, M. Tong, N.M. Harrison, Additive Manufacturing (2023) 61, https://doi.org/10.1016/j.addma.2022.103275.
[46] M.T. Hutchings, Nondestructive Testing and Evaluation 5 (5–6) (2007) 395–413, https://doi.org/10.1080/02780899008952981.